Research Article Vol. 30, No. 12 / 6 Jun 2022 / Optics Express 21710

Optics EXPRESS

Multimode soliton collisions in graded-index optical fibers

YIFAN SUN,[1,*] MARIO ZITELLI,[1] MARIO FERRARO,[1] FABIO MANGINI,[1] PEDRO PARRA-RIVAS,[1] AND STEFAN WABNITZ[1,2]

[1] *Department of Information Engineering, Electronics and Telecommunications, Sapienza University of Rome, Via Eudossiana 18, 00184 Rome, Italy*
[2] *CNR-INO, Istituto Nazionale di Ottica, Via Campi Flegrei 34, 80078 Pozzuoli, Italy*
[*] *yifan.sun@uniroma1.it*

Abstract: In this work, we unveil the unique complex dynamics of multimode soliton interactions in graded-index optical fibers through simulations and experiments. By generating two multimode solitons from the fission of an input femtosecond pulse, we examine the evolution of their Raman-induced red-shift when the input pulse energy grows larger. Remarkably, we find that the output red-shift of the trailing multimode soliton may be reduced, so that it accelerates until it collides with the leading multimode soliton. As a result of the inelastic collision, a significant energy transfer occurs between the two multimode solitons: the trailing soliton captures energy from the leading soliton, which ultimately enhances its red-shift, thus increasing temporal separation between the two multimode solitons.

1. Introduction

Solitons are nonlinear waves with particle-like behavior, with intriguing nonlinear dynamics. Solitons are ubiquitous in physics: they appear in different contexts, ranging from fluids to plasmas [1], Bose-Einstein condensates [2], and nonlinear lattices [3]. In fiber optics, temporal solitons form due to a balance between nonlinear and dispersive effects. For ultrashort solitons (e.g., for durations <100 fs), the soliton spectrum becomes so broad, that the longer-wavelength spectral components experience Raman amplification, at the expense of shorter-wavelength components. As a result, a continuous downshift of the mean frequency of the propagating soliton occurs [4]. This phenomenon is referred to as the Raman-induced soliton self-frequency shift (SSFS). The latter has been studied extensively [5], and many applications have been demonstrated, including wavelength-tunable pulse femtosecond sources [6], analog-to-digital converters [7], and tunable delay lines [8].

As the input pulse energy increases, higher-order solitons can be formed: these pulses have no binding energy, so that they are unstable against higher-order dispersion and break-up into individual fundamental solitons [9]. The resulting fundamental solitons are subject to interaction forces: this is a problem of long-standing interest, thanks to the richness of its associated physical effects [10]. Soliton interactions have been extensively theoretically studied [11] in several different contexts [12–18]. For example, soliton interactions play an important role in the formation of optical rogue waves [19–21], rogue solitons [22], and supercontinuum generation [23].

Manipulating soliton dynamics is a key challenge for many applications of solitons and solitary waves. In particular, many efforts were made for controlling the SSFS, e.g., for suppressing it by means of a negative dispersion slope [24] or self-steepening [25]. On the other hand, the SSFS can be enhanced by using tapered fibers [26], photonic crystal fibers [27], and metamaterials [28]. The SSFS can also be controlled by using specially tailored Airy pulses [29]. These studies mostly focus on the modification of dispersion and nonlinearity of a waveguide, because the

#459447 https://doi.org/10.1364/OE.459447
Journal © 2022 Received 28 Mar 2022; revised 27 Apr 2022; accepted 6 May 2022; published 1 Jun 2022

relation between them affects the soliton properties, such as its temporal duration and power. Therefore, for a given waveguide [e.g., a singlemode fiber (SMF)], the most convenient and direct way to adjust the amount of SSFS (Ω_R) is to control the propagation length z and the soliton power P. The SSFS adjustment relation satisfies $\Omega_R \propto T_0^{-4} z \propto P^2 A_{\text{eff}}^{-2} z$, where T_0 is the soliton duration, and A_{eff} is the transverse effective mode area of the SMF.

The advent of multimode fibers (MMFs) unlocked the spatial degrees of freedom in nonlinear fiber optics [30]. In recent years, various spatiotemporal nonlinear dynamical phenomena were intensively studied, mostly using graded-index (GRIN) MMFs. These include, for example, Kerr beam self-cleaning [31,32], geometric parametric instability (GPI) [33], spatial self-imaging [34,35], spiral emission [36], multimode solitons (MMS) [37–39], spatiotemporal mode-locking [40], and soliton molecules in MMF mode-locked lasers [41].

In contrast to the case of SMFs, in GRIN fibers MMS with the same initial temporal shape can experience different nonlinear dynamics, depending on their modal composition: this is due to the fact that modes have different effective areas, hence nonlinear coefficients. As we shall see in this work, the multimode nature of MMS provides an additional flexibility in the control of their SSFS. This can be achieved by properly managing the input modal composition of the MMS, which is obviously something that cannot be done with their singlemode counterparts. Moreover, in terms of SSFS, multimode Raman solitons with different mode compositions may exhibit different amounts of SSFS Ω_R, for the same peak power P and at the same propagation length z, as shown in Fig. 1. Generally, MMSs with larger SSFS exhibit a larger group delay. Such a different SSFS entails that the MMS have different group velocities. This provides the necessary condition for observing the temporal collision of two MMSs with similar peak power P at a given fiber position.

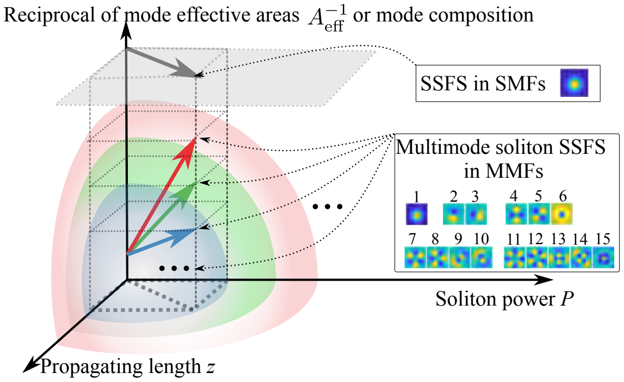

Fig. 1. Conceptual comparison of SSFS dependence for SMF and GRIN fibers. The SSFS of a soliton in a SMF depends on the soliton power P and propagation length z. Whereas multimode solitons carrying modes with different mode effective areas exhibit an additional dependence of SSFS on mode composition.

In our present study we unveil the previously undisclosed complex nonlinear dynamics of MMS interactions in GRIN optical fibers. Under appropriate input coupling conditions, one obtains that the fission of a femtosecond input pulse generates two separate MMSs. For relatively low input pulse energies, the SSFS of the two MMSs increases, as the input pulse energy grows larger. Unexpectedly we found out that, above a threshold value of input energy, the trailing MMS reduces its rate of SSFS, in spite of the growing input pulse energy. As a result, a temporal collision with the leading MMS may occur: this collision is inelastic, which means that energy exchange between the solitons takes place. Specifically, after the collision the trailing soliton gains energy at the expense of the leading soliton: hence, the SSFS (or group delay) of the trailing soliton grows larger, which leads to temporal separation among the two MMSs.

This paper is organized as follows. In section 2, the model and physical parameters are introduced. Next, we study the properties of a soliton carrying only one specific mode in a GRIN fiber, by considering its group velocity (GV), group delay (GD) and SSFS. Next, the dynamics of a two-MMS collision originating from high-order MMS fission is theoretically studied. Finally, a detailed example of MMS temporal collision occurring during propagation along the GRIN fiber is numerically analyzed. Section 3. introduces the experimental setup and results. We reproduce the predicted soliton collision features by varying the input pulse energy. Finally, Section 4. draws the conclusions of the manuscript.

2. Model and simulations

2.1. Model and parameters

The model we used to describe soliton propagation in GRIN MMFs is based on the generalized multimode nonlinear Schrödinger equations (GMMNLSEs) [42,43]. The field envelope in the fiber can be expanded on the basis of its eigenmodes:

$$\mathcal{E}(x,y,z,t) = \sum_{p=1}^{N} F_p(x,y)A_p(z,t), \tag{1}$$

where $F_p(x,y)$ are the transverse mode patterns. For GRIN fibers, the eigenmodes are the Laguerre-Gauss (LG) modes. These modes are orthogonal; we normalize them, so that the mode amplitudes A_p are expressed in $\sqrt{\mathrm{W}}$. The evolution of the field envelope A_p of mode p is governed by the GMMNLSEs [42,43]:

$$\frac{\partial A_p(z,t)}{\partial z} = \mathcal{D}\{A_p(z,t)\} + \mathcal{N}\{A_p(z,t)\}, \tag{2}$$

where the dispersion terms are

$$\mathcal{D} = i(\beta_0^{(p)} - \beta_0^{(1)})A_p - (\beta_1^{(p)} - \beta_1^{(1)})\frac{\partial A_p}{\partial t} + i\sum_{q\geq 2}^{4} \frac{\beta_q^{(p)}}{q!}\left(i\frac{\partial}{\partial t}\right)^q A_p, \tag{3}$$

and the nonlinear terms read as

$$\begin{aligned}\mathcal{N} = i\frac{n_2\omega_0}{c}\left(1+\frac{i}{\omega_0}\frac{\partial}{\partial t}\right)\sum_{l,m,n}^{N}[(1-f_R)S_{plmn}A_lA_mA_n^* \\ +f_RS_{plmn}A_l\int_{-\infty}^{t}\mathrm{d}\tau h_R * (A_m(z,t-\tau)A_n^*(z,t-\tau))].\end{aligned} \tag{4}$$

The GRIN fiber we used in simulations and experiments has a 50 μm diameter core with a parabolic refractive index profile, where the difference between the core center and the cladding is $\Delta n = 0.015$. The field profile $F_p(x,y)$ for mode p and the corresponding q-th derivative of the propagation constant $\beta_q^{(p)}$ were directly calculated on the basis of the parabolic index distribution of the fiber [44] [see details in Sec. 1 in Supplemental Document]. In the top panel of Fig. 2, we draw $F_p(x,y)$ for $p = 1, \ldots, 15$. The nonlinear mode coupling coefficients are

$$S_{plmn} = \frac{\int \mathrm{d}x\mathrm{d}y F_pF_lF_mF_n}{\sqrt{\int \mathrm{d}x\mathrm{d}y F_p^2 \int \mathrm{d}x\mathrm{d}y F_l^2 \int \mathrm{d}x\mathrm{d}y F_m^2 \int \mathrm{d}x\mathrm{d}y F_n^2}}. \tag{5}$$

For the nonlinear response of the fiber, we consider the standard parameters of silica [45,46]: the nonlinear index $n_2 = 2.7 \times 10^{-20}\ \mathrm{m^2W^{-1}}$, the coefficient of the Raman contribution to the

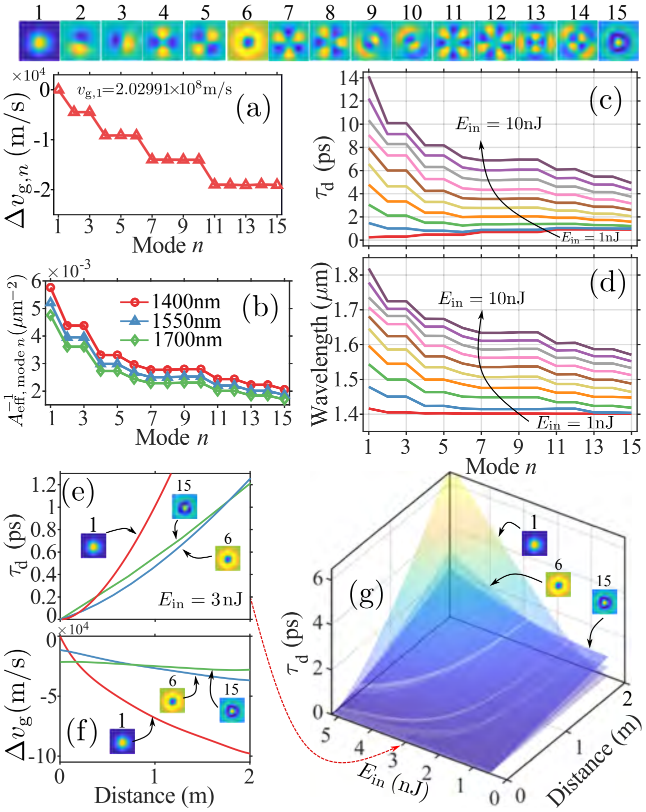

Fig. 2. Top panel: LG modes of the GRIN fiber used in this work. For compactness of notation, we use a single index n to refer to these modes. (a,b) Linear relative group velocity in (a) $\Delta v_{g,n} = (\beta_1^{(n)})^{-1} - (\beta_1^{(1)})^{-1}$ and inverse of mode effective area $A^{-1}_{\text{eff, mode } n}$ in (b) vs. mode index n. (c,d) Group delay and wavelength of singlemode solitons emerging from a 2 m long fiber, as a function of mode index n. (e,f) Group delay τ_d and relative group velocity Δv_g of singlemode solitons with mode $n = 1, 6, 15$, as a function of propagation distance, when the input pulse energy is $E_{in} = 3$ nJ. (g) Evolution of group delay τ_d of singlemode solitons (mode $n = 1, 6, 15$) vs. input energy E_{in} and propagation distance z.

Kerr effect $f_R = 0.18$, the Raman response is h_R, with the two time constants $\tau_1 = 12.2$ fs and $\tau_2 = 32$ fs [46].

For the simulations presented in the following sections, the fiber length is 2 m. Dispersion coefficients with up to $N = 4$ in Eq. (3) are taken into account. The input pulses have $T_0 = 70$ fs FWHM duration, and $\lambda_0 = 2\pi c/\omega_0 = 1400$ nm center wavelength, but may have different mode contents, as described in the following. Equations (2–4) are solved by the so-called massively parallel algorithm (MPA) [43] with the following parameters: step size $\Delta z = 25\ \mu$m, parallelization extent $M = 20$, temporal resolution $\Delta t = 4.89$ fs, and temporal window $T = 20$ ps.

2.2. Group velocity of singlemode soliton in GRIN fiber

Let us start by considering the simplest case of a soliton carried by a single specific mode in the MMF. This case is helpful for understanding the mechanism of proper MMS collisions. Temporal soliton collision is a strong interaction of two solitons. A necessary condition for a collision to occur is that the trailing soliton propagates faster than the leading one, so that the two solitons gradually approach each other.

In the absence of nonlinearity, the GV of a propagating pulse mainly depends on the first-order dispersion coefficient: $v_{g,n} = (\beta_1^{(n)})^{-1}$. Since in GRIN fibers the $\beta_1^{(n)}$ values for the different modes are equally spaced, the relative GV $\Delta v_{g,n} = (\beta_1^{(n)})^{-1} - (\beta_1^{(1)})^{-1} \approx (\beta_1^{(1)} - \beta_1^{(n)})(\beta_1^{(1)})^{-2}$ are almost equally spaced, as shown in Fig. 2(a). Therefore, in the absence of nonlinear effects, a pulse carried by a low-order mode (LOM) propagates faster than a pulse carried by high-order modes (HOMs). These different velocities can be easily identified by checking the group delay τ_d [temporal shift of the pulse peak, with respect to a reference frame moving with the fundamental mode velocity $v_\mathrm{F} = 1/\beta_1^{(1)} = 2.029 \times 10^8$ m/s]. By solving Eq. (2), we calculated the values of τ_d for different singlemode pulses as a function of their mode index n, emerging from a 2 m long GRIN fiber. We carried out the calculation including the nonlinear term for different values of the input pulse energy: the corresponding results are shown in Fig. 2(c). Indeed, we can see that in the low input energy regime (e.g., for $E_\mathrm{in} = 1$ nJ), LOMs have less GD than high-order ones.

However, as the input pulse energy increases, the GD of singlemode solitons is affected by the presence of (Raman) nonlinearity. We have checked that the output pulses are not temporally broadened by dispersion when $E_\mathrm{in} \geq 2$ nJ, which indicates that a soliton is formed, since the linear dispersion length of the fiber is $L_\mathrm{D} = T_0^2/|\beta_2| = 0.034\,\mathrm{m} \ll 2\,\mathrm{m}$. In Fig. 2(c), we can see that the GD of LOM solitons increases faster with input energy, with respect to the case of HOM. Finally, whenever $E_\mathrm{in} \geq 3$ nJ, LOM solitons have a larger GD with respect to HOM. This means that, soliton GVs change with the input energy, so that by choosing a suitable input energy, two singlemode solitons in different modes could have the same GD at the fiber output.

In the spectral domain, the SSFS of solitons exhibits a similar behavior to that of τ_d, as shown in Fig. 2(d). In fact, the mode distributions of the GD and the SSFS for different input pulse energies have a similar trend, see Fig. 2(c,d). This is because of the different effective mode areas $A_{\mathrm{eff},n}$, which lead to different strengths of their nonlinearity. The strength of the Raman effect is proportional to the mode overlap factors S_{plmn} [see Eq. (4)]. For a singlemode soliton in GRIN fibers, this term in Eq. (5) is simplified, and it is equal to the inverse of the mode effective area $S_{nnnn} = A^{-1}_{\mathrm{eff,\,mode}\,n}$, which is shown in Fig. 2(b): the resulting decrease of the inverse effective area with mode n is in agreement with the corresponding decrease of GD and SSFS, which are shown in Figs. 2(b,d). In addition, the mode effective area increases with the wavelength [see Fig. 2(c)]. This indicates the nonlinearity strength reduces as the wavelength increases.

It is also interesting to consider how the velocity of singlemode solitons varies upon propagation along the GRIN MMF. One example of temporal delay $\tau_\mathrm{d}(z)$ of a singlemode soliton as a function of distance z for modes 1, 6 , or 15, respectively, is shown in Fig. 2(e), for an input pulse energy $E_\mathrm{in} = 3$ nJ. The local group velocity along distance z can be calculated as

$$v_\mathrm{g}(z) = \frac{\mathrm{d}z}{\mathrm{d}t} = \left(\frac{\mathrm{d}(t_\mathrm{frame} + \tau_\mathrm{d})}{\mathrm{d}z}\right)^{-1} = \left(\beta_1^{(1)} + \frac{\mathrm{d}\tau_\mathrm{d}}{\mathrm{d}z}\right)^{-1}. \tag{6}$$

This leads to the relative local group velocity with respect to a reference frame moving with the fundamental mode speed

$$\Delta v_\mathrm{g}(z) = v_\mathrm{g}(z) - (\beta_1^{(1)})^{-1} \approx -(\beta_1^{(1)})^{-2}\frac{\mathrm{d}\tau_\mathrm{d}}{\mathrm{d}z}. \tag{7}$$

The values of $\Delta v_\mathrm{g}(z)$ for the three different monomode solitons are shown in Fig. 2(f). As we can see in Fig. 2(f), initially (i.e., at $z = 0$) all solitons have the GVs which are predicted according to Fig. 2(a). The GV of the soliton carried by mode $n = 1$ is the largest in the beginning of the fiber but, due to the slowing down induced by the SSFS, it also experiences the fastest decay [see Fig. 2(f)]. This gives the soliton carried by mode $n = 6$ (or mode $n = 15$) the chance to catch up with the mode $n = 1$ soliton at 0.2 m (or 0.38 m) [see Fig. 2(e)]. The solitons carried by mode $n = 6$ and $n = 15$ also have the same GD at 1.73 m. These equal GD points vary when the input energy changes. The evolution of the GD τ_{d} as a function of both input pulse energy E_{in} and propagation distance z is shown in Fig. 2(g). Here the three white lines represent points of equal GDs for any pair of singlemode solitons for a specific input pulse energy value. This indicates that two propagating solitons carried by different modes have the possibility to temporally overlap at a specific position in the fiber, owing to the nonlinear dependence of their GV.

For MMSs, the properties of the GV, GD and SSFS are more complex than in the case of singlemode solitons. For a MMS, the GD (under the influence of SSFS) not only depends on the values of peak power, propagation length, and mode effective area, but it also varies with its specific mode composition. As discussed in details in Sec. 3 in Supplemental Document, MMSs carrying a larger portion of LOMs experience a larger amount of SSFS and GD with respect to MMSs carried by HOM. Therefore, two MMSs with different mode compositions, will exhibit a different evolution of their GVs. As a result, under suitable conditions the two MMSs can acquire the same GD at a specific position in the fiber. For two MMSs originating from a MMS fission, these equal GD points provide the necessary condition for their collision, as we are going to see in the next section.

2.3. Numerical simulations of soliton collision

Because of the previous considerations, we may expect that the fission of a high-order MMS could provide the testbed for the collision of two separate MMSs, carrying different mode contents. In this section we investigate evolution of MMSs. For doing that, we shall keep the same simulation parameters as before, except for increasing the input pulse energy, and varying the mode composition of the input pulse.

As a matter of fact, setting the appropriate mode composition for the input pulse is a critical condition for controlling the occurrence of a soliton collision. In order to quantify the input mode content for a given input laser beam, we decomposed the input Gaussian beam with full-width-at-half-maximum (FWHM) w, and offset s with respect to the fiber axis, on the basis of the LG modes. These two parameters are normalized with respect to the FWHM $w_{\mathrm{LG}_{01}} = 8.79$ μm of the fundamental mode $|F_1(x,y)|^2$ at 1400 nm. Therefore, by tuning the dimensionless parameters $r_{\mathrm{w}} = w/w_{\mathrm{LG}_{01}}$ and $r_{\mathrm{s}} = s/w_{\mathrm{LG}_{01}}$, we can sweep over different modal compositions [Details about the dependence of the input mode content on these parameters can be found in Sec. 2 of the Supplemental Document]. Generally, the larger the beam size w, the higher the mode content of the input beam.

2.3.1. Output field evolution with input pulse energy

We investigate by numerical simulations how the output field evolves with input pulse energy, as the input coupling conditions are varied. Figure 3(a) shows a first example of the input pulse energy dependence of the output spectra from a 2 m GRIN fiber. Here we consider injecting a beam with $r_{\mathrm{w}} = 2$, $r_{\mathrm{s}} = 0$. As it can be seen, in the low energy regime (E_{in}<6 nJ), only one MMS (S1) is formed. Whereas, a second MMS (S2) appears at E_{in}>6 nJ, owing to higher-order soliton fission. Both of these MMSs experience larger GD and SSFS, as the input energy increases [see Visualization 1]. As a result, the output wavelengths of S1 and S2 are 2.1 μm and 1.75 μm for $E_{\mathrm{in}} = 25$ nJ, respectively.

By introducing a higher-order mode content at the fiber input, i.e., $r_{\mathrm{w}} = 2.8$, $r_{\mathrm{s}} = 0.5$, we obtain the result shown in Fig. 3(b). Here the second soliton S2 appears at the same input energy as before, i.e., E_{in}>6 nJ. Unexpectedly, when E_{in}>17 nJ, the two MMSs exhibit a completely different dynamics, when compared with the one in Fig. 3(a): namely, now S1 undergoes a reduced amount of SSFS, as the input energy increases. This brings the two MMSs both spectrally (and temporally) closer and closer to each other, however they remain spectrally distinct [see Visualization 2]. Whereas, for E_{in}>24 nJ the two MMSs start to separate again. In addition, the

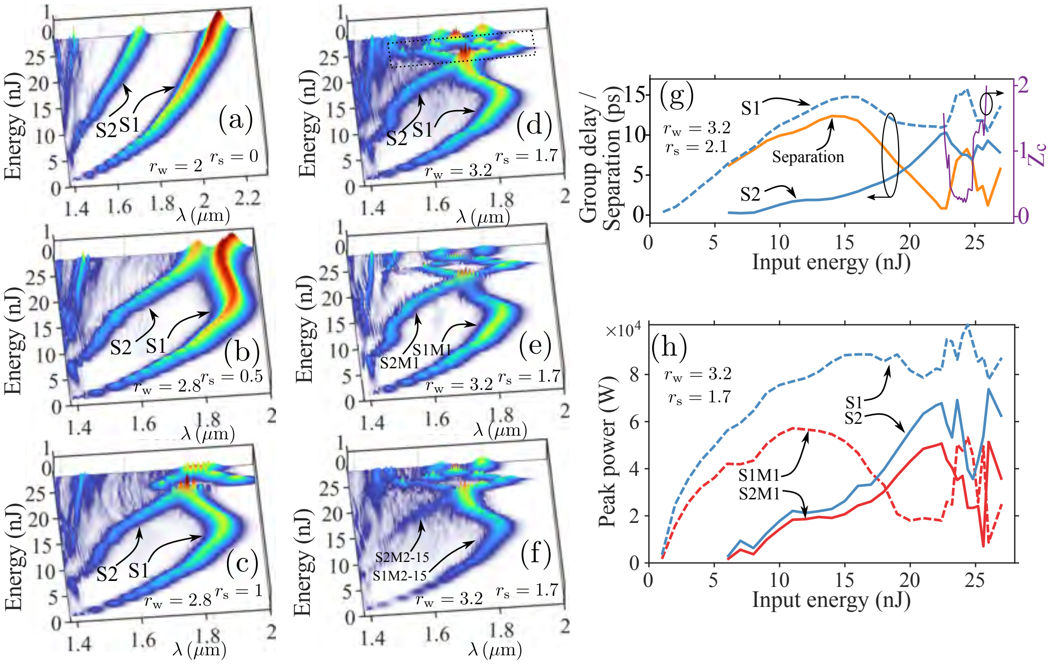

Fig. 3. (a-d) Simulation results of output spectra vs. input pulse energy for an input Gaussian beam width $r_w = 2$ and center offset $r_s = 0$ in (a), $r_w = 2.8$ and $r_s = 0.5$ in (b), $r_w = 2.8$ and $r_s = 1$ in (c) and $r_w = 3.2$ and $r_s = 1.7$ in (d). The two MMSs are marked by S1 and S2. (e,f) Spectrum evolution of mode 1 (S1M1 and S2M1) and of the remaining 14 modes (S1M2-15 and S2M2-15) for the simulation in (d) are shown in panels (e) and (f), respectively. (g) Soliton GDs, their separation and the propagation distance Z_c where the collision occurs for the simulation in (d), vs. input pulse energy. (h) Peak power of S1 and S2 and their fundamental mode peak power (S1M1 and S2M1), vs. input pulse energy.

output wavelengths of S1 and S2 are 1.9 μm and 1.8 μm at 25 nJ: the former is smaller than what previously reported in Fig. 3(a).

By further increasing the HOM content at the fiber input, i.e., when setting $r_w = 2.8$, $r_s = 1$, we obtain the result shown in Fig. 3(c) [see temporal and spectral evolution of the two MMSs along the fiber in Visualization 3]. As can be seen, in this case for all input energies S1 experiences a much smaller SSFS when compared with the case of Fig. 3(b): as a result, S1 and S2 fully spectrally overlap at around $E_{in} = 25$ nJ. Upon further increasing the input energy, the spectra of the two MMSs separate, until they overlap again for $E_{in} = 27$ nJ. The two spectral fringe patterns at $E_{in} = 25$ nJ and $E_{in} = 27$ nJ imply that the two MMSs are very close to each other in the temporal domain.

By acting on the input mode composition, one may further tune the interactions between two MMSs. As an example, in Fig. 3(d), we report the case of $r_w = 3.2$, $r_s = 1.7$ [see their evolution along the fiber in Visualization 4]. As one can visibly appreciate, in this case the dynamics is similar to that of Fig. 3(c); however, the collision wavelength and energy are reduced down to 1.72 μm and 22.5 nJ, respectively. Thus we can see that by increasing the input HOM content, one may shift the collision point to occur at shorter wavelengths and lower energies. This tendency is similar to the the behavior that we previously described for singlemode solitons in Fig. 2(d).

In order to reveal the physical mechanism leading to the unexpected evolution of the SSFS for S1, and the resulting soliton collisions, it is necessary to analyze how the mode content of the MMS evolves as the input energy is varied. In order to do that, we decompose the total spectrum of Fig. 3(d) into its different modal components. In particular, this permits to highlight the specific contribution of mode 1. The latter is shown in Fig. 3(e), whereas the remaining mode content (ranging from mode 2 up to mode 15) is illustrated in Fig. 3(f). These spectra are labeled S1M1, S1M2-15 for S1 and S2M1, S2M2-15 for S2, respectively. By comparing Figs. 3(e,f), we can ascribe the reduced SSFS of S1 to its decreased fundamental mode content S1M1. Indeed, the latter progressively reduces when increasing the input energy, i.e., at >16 nJ. To the contrary, the power increase in HOM content S1M2-15 does not provide a sufficient boost to the SSFS.

In order to quantitatively estimate the role of the modal content on the temporal evolution of MMSs, in Fig. 3(g) we plot the evolution with input pulse energy of the temporal GD (and temporal separation) of S1 and S2, respectively. Whereas in Fig. 3(h) we show the corresponding evolution of peak power of S1, S2, S1M1 and S2M1. As we can see, whenever $E_{\text{in}}<22.5$ nJ, the peak power of S1 and S2 increases as the input energy grows larger; for any input energy value, the power of S1 is larger than that of S2. However, the power of S1M1 starts to dramatically decrease at $E>15$ nJ. Correspondingly, the GD and SSFS experienced by S1 are both reduced, until they become comparable to the values of S2. This leads to generating temporally overlapping solitons when $E = 22.5$ nJ, thus further confirming that the fundamental mode content plays a key role in determining the properties of the MMSs.

It is worth to mention that, in the input energy range between $22.5\,\text{nJ}<E_{\text{in}}<26\,\text{nJ}$, the fiber position where the collision of two MMSs occurs depends on the specific input energy value. Notably, for the specific cases of $E_{\text{in}} = 22.5$ nJ or $E_{\text{in}} = 26$ nJ, the MMS collision occurs at 2 m. In Fig. 3(g) we plot the propagation distance Z_c where the two MMSs have the closest temporal separation, i.e. the collision occurs, as a function of input pulse energy [see evolution of the temporal and spectral intensity profiles at different fiber lengths in Visualization 4]. We found that the largest value of SSFS for S1 occurs when the input energy is 24 nJ, which leads to MMS collision after 0.3 m of propagation. This is because, under this peculiar input condition, S1 gains energy from S2 after a minimal distance of propagation. Therefore, S1 propagates for the longest available fiber length, thus accumulating the maximum SSFS. For the other collision cases in this energy region, the smaller the SSFS (or GD) of S1, the longer the distance where collision occurs. One may expect that, for a longer fiber, collisions may occur for a wider energy range. A particular evolution of two colliding MMSs along the fiber is discussed in the next section.

2.3.2. Field evolution inside the GRIN fiber

So far, we have shown the spectral features of the field which is observed at the fiber output. Thus, at this point, one may naturally wonder: how do MMSs exactly collide inside the fiber?

An example of soliton collision in the fiber with the same parameters ($r_{\text{w}} = 3.2$, $r_{\text{s}} = 1.7$) of Fig. 3(d), and the input energy $E_{\text{in}} = 22.7$ nJ, is depicted in Fig. 4(a). A 70 fs pulse is injected at the beginning of the fiber, and it splits into two MMSs, marked as S1 and S2. The GVs of both solitons are slower than the moving speed of the temporal reference frame. As a consequence, we can see that their temporal delay increases, as both solitons propagate along the fiber. In order to better display the temporal evolution of the solitons around the collision region [which occurs between 1.1 m and 2 m, see the grey dashed parallelogram in Fig. 4(a)], the total fields (S1,S2), the projection on mode $n = 1$ (S1M1,S2M1) and the sum of the remaining modes (S1M2-15, S2M2-15) are processed by temporal translations, and re-plotted in Fig. 4(c-e). Here we can clearly see the power exchange between the two MMSs, as they approach each other, and collide around 1.6 m.

The evolution of the spectrum vs. propagation distance is shown in Fig. 4(b). We may note the occurrence of an interference pattern in the spectral domain, which occurs in correspondence with the collision point. The two interacting solitons can be better visualized by looking at spectrograms computed at 1 m, 1.3 m, 1.6 m, and 2 m, respectively, as reported in the insets of Fig. 4(a). We may notice that the two solitons have almost the same value of SSFS before

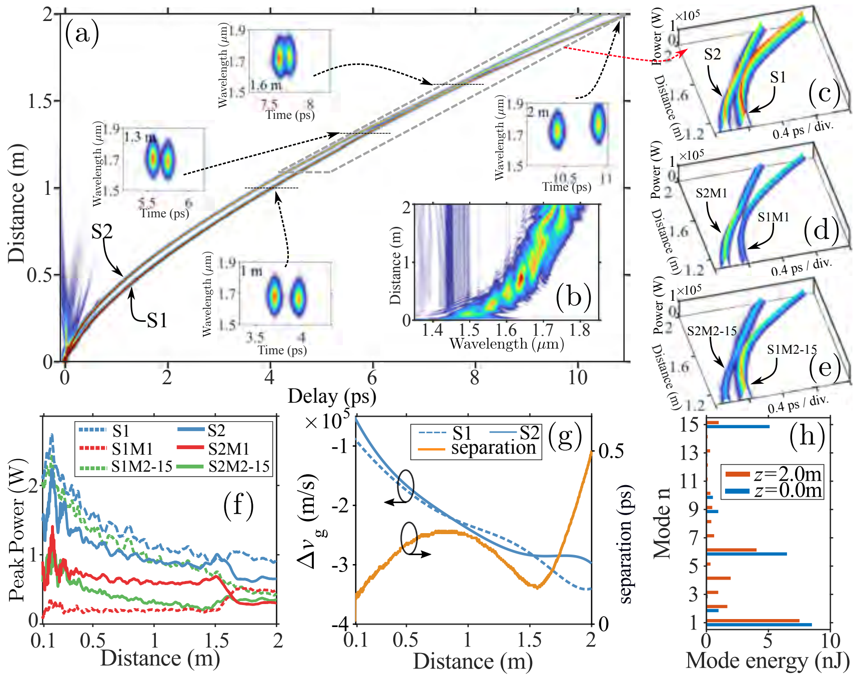

Fig. 4. One example of MMS evolution in the fiber as in Fig. 3(d) (r_w = 3.2, r_s = 1.7), when input pulse energy is E_in = 22.7 nJ. (a,b) Temporal and spectral evolution of field intensity as a function of propagation length z, respectively. Spectrograms at specific fiber lengths are inserted in (a). (c-e) The temporal evolutions of total fields, mode 1 (M1), and sum of mode 2-15 (M2-15) correspond to the region of gray dashed parallelogram in (a). (f,g) Evolution of total peak powers of solitons (S1, S2), their mode peak powers (S1M1, S2M1, S1M2-15, S2M2-15) in (f), and the relative group velocities of S1 and S2 and their temporal separation in (g) as a function of propagation length z. (h) Mode energy distribution comparison between the input and the output of the fiber.

the collision occurs. Conversely, after the collision, S1 acquires energy from S2, which leads to boosting both its SSFS and GD. The entire evolution of the temporal intensity profile (with corresponding spectrograms) along the fiber is shown in Visualization 5.

In order to better display the influence of the mode content on the evolution of a MMS, in Fig. 4(f) we plot the peak power of both S1 and S2, along with their fundamental (S1M1, S1M1) and HOM content (S1M2-15, S2M2-15), as a function of the propagation distance. Furthermore, by extracting from Fig. 4(a) the soliton delay $\tau_\mathrm{d}(z)$ as a function of propagation distance z, we calculated the relative GV $\Delta v_\mathrm{g}(z)$ by using Eq. (7), as well as the temporal separation between the two solitons, both which are plotted in Fig. 4(g).

Based on Fig. 4(f,g), we may highlight the following three main phases of the collision process: (i) *Before the collision.* After the fission which takes place at 0.1 m, the input pulse is splitted into two separate MMSs. As a result, S2 is generated, which initially propagates faster than S1 [see Fig. 4(g)]. The peak power of both S1 and S2 exhibits an asynchronous oscillatory behavior [see Fig. 4(f)]. As discussed before, the SSFS and the GD are influenced by the Raman effect, whose impact is dominated by the contribution of the fundamental mode. Therefore, although the total power of S2 is smaller than that of S1, the peak power of S2M1 is larger than that of S1M1. Thus, S2 experiences a larger Raman effect than S1. Hence, we see that the GV of S2 reduces faster than that of S1, until it gets even smaller that the velocity of S1 at 0.86 m. (ii) *At* *the Collision.* As a result of the GV dynamics, the two MMSs eventually collide at 1.6 m. It is worth mentioning that the occurrence of a collision can be fully ascribed to the multimode nature of S1 and S2. As a matter of fact, when considering soliton fission in a singlemode fiber, the trailing soliton S1 with a larger energy can never accelerate and reach S2, which removes the possibility of any soliton collision to occur. Due to the inelastic collision, S1 gains energy from S2. Specifically, the energy of S1M1 increases, while S2M1 decreases. (iii) *After the collision*. Thanks to its increased fundamental mode content, now S1 undergoes a larger SSFS, and a lower GV with respect to S2. Therefore, the two MMSs progressively separate in time, without experiencing any further interaction. Finally, in Fig. 4(h) we compare the mode content at the fiber input and output. Here, we can see that the radial modes (modes with $n = 1, 6, 15$) lose their energy, which is conversely acquired by non-radial modes.

It is worth mentioning that such collision is harder to be observed in step-index fibers due to their larger modal dispersion. For example, in Fig. 2(a), for the GRIN fiber, the linear group velocity difference between radial modes is $\Delta v_{g,n=6} \approx 10^4$ m/s. This group velocity difference can be reduced when increasing the input pulse energy due to the Raman nonlinearity [See Fig. 2(c): here the group delay difference for different modes at the fiber output reduces when increasing the input energy from 1 nJ to 10 nJ]. Since this group velocity difference is small, it is very sensitive to modifications by the Raman nonlinearity. This provides a larger possibility for the temporal collision of two MMSs. To the contrary, for fibers with larger modal dispersion, for example, the step-index fiber with the same radius $R = 25$ μm, the group velocity difference among radial modes is around $\Delta v_g \approx 10^5$ m/s. In addition, the fundamental mode effective area of the step-index fiber is five times larger than that of the GRIN fiber. Such a bigger group velocity difference and weaker nonlinearity make it harder to observe the soliton collision of two MMSs.

3. Experiments

In order to confirm the simulation results in Sec. 2, we have carried out a set of experimental tests. Let us start by describing the experimental setup, before reporting the observations which closely match our theoretical predictions.

3.1. Experimental setup

In our experiments, we used the same type of GRIN fiber as previously described. The experimental setup is shown in Fig. 5. Linearly polarized optical pulses (with 70 fs temporal duration, 1400 nm center wavelength and 100 kHz repetition rate) are emitted by a hybrid optical parametric amplifier (Light Conversion ORPHEUS-F), pumped by a femtosecond Yb-based laser (Light Conversion PHAROS-SP-HP). The input pulse energy is controlled by rotating the computer motorized $\lambda/2$ waveplate, as shown in Fig. 5. A beam splitter (BS) is used for monitoring the input power by means of a power meter (Thorlabs PM16-122). The laser beam, which has a Gaussian profile ($M^2 = 1.1$), is injected by means of a 50 mm lens into the GRIN fiber, with a diameter of approximately 30 μm at $1/e^2$ of peak intensity on the fiber input facet. At the fiber output, the beam is collected by an achromatic microlens, and separated into three paths, in order to measure the output beams near-field, their spectra, as well as the MMS temporal separation, by using an InGaAs camera (Hamamatsu C12741-03), a spectrometer (Fastlite Mozza), and an autocorrelator (APE pulse check 50), respectively. The latter is appropriately equipped with a 1500 nm longpass filter, in order to extract the Raman soliton out of the total output spectrum.

The accurate control of the coupling conditions of the input pulses into the GRIN fiber is a critical condition for studying the dynamics of MMS collisions. Whenever the input beam is symmetrically coupled at the center of the fiber, one obtains a spectral evolution which is similar to the case reported in the simulation of Fig. 4(a). Therefore, in order to unveil the peculiar MMS collision-induced spectral dynamics, we offset the input laser beam by around 7 μm with respect

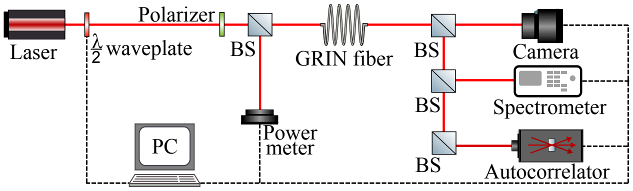

Fig. 5. Sketch of the experimental set-up.

to the center of the fiber core. This leads to the generation of MMSs with far greater HOM content at the beginning of the fiber. This beam offset and the value of the input pulse energy need to be finely tuned, until we find out the occurrence of an interference fringe spectrum. As we have seen before, this is a signature of the collision of two MMSs at the fiber output. Once this is done, the only parameter to be adjusted is the input pulse energy, in order to record the corresponding nonlinear evolution of the output spectrum.

3.2. Experimental results

Since we aim at experimentally retrieving the simulation predictions of Sec. 2, we used $L_1 = 2$ m of GRIN fiber. Next, we further confirmed the generality of our findings by using a $L_2 = 10$ m long GRIN fiber span.

In Fig. 6 we show the results of our experiments with the 2 m fiber. Specifically, in Figs. 6(a,b) we illustrate the measured output spectra, along with their corresponding autocorrelation traces, at different input pulse energies. For $E_{\text{in}}<19$ nJ, we can clearly identify the presence of two distinct solitons, both in the spectral domain and in the temporal domain. The temporal separation of the two solitons can be inferred by the autocorrelation traces in Fig. 6(c). Figure 6(a) shows that, when E_{in} increases, the spectra of the two MMSs get progressively closer in the frequency domain. However, one cannot clearly distinguish the presence of two separate solitons by just examining the fringe pattern which appears in the spectrum, for energies between 20 nJ$<E_{\text{in}}<$21 nJ. This is why we need to complement our spectral measurements with the temporal domain results of Figs. 6(b,c), which reveal the presence of two MMSs with a separation of less than 0.5 ps for $E_{\text{in}} = 20.5$ nJ. For 21 nJ$<E_{\text{in}}<$23 nJ, we detected the presence of a single dominant soliton in the middle of autocorrelation trace of Fig. 6(b). Nevertheless, this figure also shows the occurrence of a weak peak at ±4 ps for input energies in the same range 21 nJ$<E_{\text{in}}<$23 nJ. This indicates that the two solitons do not overlap in the temporal domain at the fiber output. To the contrary, they are well-separated in time after the occurrence of a collision at a previous position $Z_c<L_1$ in the fiber. The presence of well-separated solitons is confirmed by the occurrence of distinct spectra in Fig. 6(a) in the same input energy range. The two solitons are separated at the fiber output because the trailing soliton S1 acquires energy from the leading soliton S2 at the collision point in the fiber. This leads to enhancing the red-shift for S1. For input energies larger than the collision region (i.e., for $E_{\text{in}}>$23 nJ), Figs. 6(b,c) shows that the two MMSs are again well-separated at the fiber output. In addition, we may note in Fig. 6(d), showing four beams and their corresponding spectra, that different MMSs exhibit a multimode transverse profile which varies with the input pulse energy.

Now, it is interesting to both qualitatively and quantitatively compare simulation and experimental results. To better show the comparison between theory and experiments, the regions where collisions occur are marked by the dashed rectangles, both for the simulation result in Fig. 3(d) and for the experimental result in Fig. 6(d). Figure 6(d) shows that the first soliton overlap point at the fiber output occurs at 1.65 μm, for an input energy of 20.5 nJ. This energy value is slightly lower than for the soliton overlap point that was found numerically at the soliton

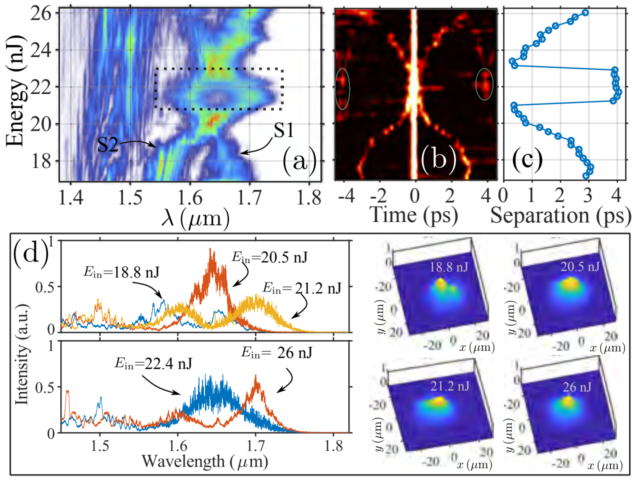

Fig. 6. Experimental results for a 2 m fiber. (a-c) Spectral evolution in (a), autocorrelation in (b), and temporal separation between the solitons vs. input energy. (d) Selection of four spectra with their corresponding output beams, for different input pulse energies as in (a).

overlap point, which occurs at 22.5 nJ [cfr. Figure 3(d)]. The small discrepancy is likely to be due to the limited number of modes which is used in simulations.

So far, we have shown spectral and temporal properties of the field emerging at the fiber output. In order to experimentally monitor the collision dynamics along the fiber, similarly to what reported by simulations in Sec. 2, one would need to carry out a cut-back experiment. However, this is a challenging task, since performing a cut-back experiment may lead to changing the bending properties of the fiber, which can be detrimental for our study. Therefore, we limit ourselves to validate our conclusions by repeating the experiments with a longer, 10 m span of GRIN fiber. In Fig. 7(a) we show the corresponding measured output spectrum, again as a function of the input energy E_{in}. As we can see, the solitons experience larger amounts of SSFS, when compared with the former result in Fig. 6(a). In a first stage (i.e., for E_{in}<6 nJ) a MMS (S1) is formed, whose wavelength increases with E_{in}. For E_{in}>6 nJ, the fission of the input pulse generates an additional MMS (S2). When E_{in} grows larger, S1 and S2 undergo different amounts of SSFS. Again, when E_{in}>20 nJ, we observed that the SSFS of S1 is reduced as the input pulse energy increases: this appears as a relative "blue-shift" in Fig. 7(b). Once again, the observed spectral evolution is qualitatively remarkably similar to simulation predictions. A spectral overlap of the two solitons is reached for $E_{in} \simeq 26.9$ nJ. The relevant output spectra, corresponding to input energies such that collision occurs at some point inside the fiber, are marked by the red dashed box in Fig. 7(b). Finally, for E_{in}>45 nJ, the two solitons S1 and S2 clearly separate again. Examples of four spectra with their corresponding beams at different values of E_{in} are illustrated in Fig. 7(b). The detailed evolution of these spectra can be seen in Visualization 6.

It is worth mentioning that, for such multimode solitons, the field intensity periodically oscillates in GRIN fibers owing to mode beating, an effect which is known as self-imaging [35]. This could result in generating a series of spectral peaks, associated with resonant dispersive radiation [47,48] in the anomalous dispersion, and with geometric-type parametric instability [33] in the normal dispersion. However, such spectral peaks are not observed in the present work, nor in our previous reports [38,39], due to the different pumping conditions. The pumping pulse in our work has much smaller energy (<30 nJ) and shorter duration (70 fs), when compared with the pumping pulses (>200 nJ and >400 fs) in Ref. [47,48]. Based on these different initial conditions, we could infer that, in our case, sideband instabilities are negligible. The possible

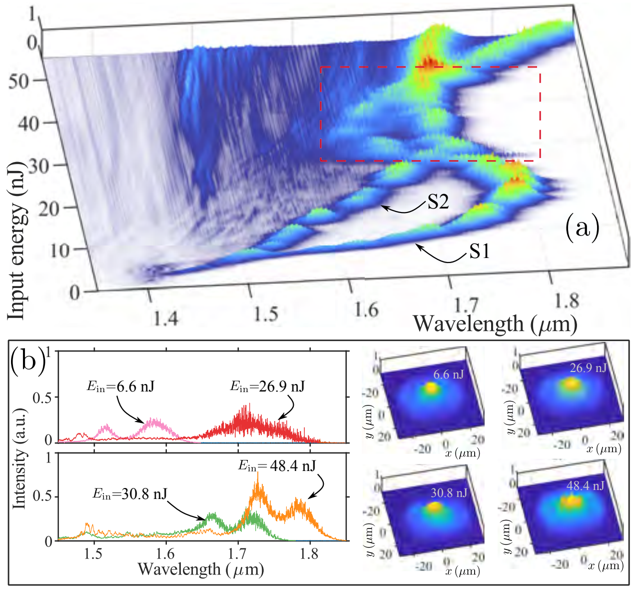

Fig. 7. Experimental results with a 10 m long GRIN fiber. (a) Spectral evolution vs. input energy. (b) Selection of four spectra and output beams, for different input energies in (a).

reasons for this could be: (1) in our case, the pumping pulse energy does not reach the level for significantly triggering the instability; (2) The interaction between dispersion, experienced by 70 fs pulses with broader bandwidth, and combined Kerr and Raman nonlinearity is the dominant effect, whose dynamics weakens the sideband instability.

4. Conclusions

To summarize, in this work we have numerically and experimentally studied the interaction of MMSs, resulting from the fission of femtosecond pulses in GRIN fibers. We have revealed the surprising result that, as a result of the variation of the MMS mode content, the SSFS of the trailing MMS is reduced, in spite of the growing energy of the input pulse. This is an anomalous behavior, which has no counterpart in the realm of singlemode fiber solitons. The physical mechanism behind such an effect is the variation, with input energy, of the mode composition of the MMS that results from the fission of the input pulse. Specifically, the fundamental mode is depleted in favour of HOMs. This results in an input energy dependence of the group velocity of the trailing MMS. As a result, an inelastic collision may occur between the two fission-generated multimode solitons. In turn, the collision leads to a redistribution of both energy and mode content between the two interacting solitons. The nonlinear collision dynamics predicted by numerical simulations is well confirmed by experiments. From a fundamental standpoint, our analysis unveils the previously undisclosed complexity of MMS interactions. Such an abrupt redistribution of energy between modes during collisions might be exploited for the design of multimode solitons with a specific modal distribution. In addition, our results deepen the current understanding of the dynamics of MMSs, which may lead to rogue wave formation, supercontinuum generation, and spatiotemporal mode-locking in multimode fiber lasers.

Funding. H2020 European Research Council (740355); H2020 Marie Skłodowska-Curie Actions (101023717); Ministero dell'Istruzione, dell'Università e della Ricerca (R18SPB8227); Sapienza Università di Roma (AR22117A8AFEF609, AR22117A7B01A2EB).

Acknowledgments. We thank L. Wright et al. for making freely available the open-source parallel numerical mode solver for the coupled-mode nonlinear Schrödinger equations [43].

Disclosures. The authors declare no conflicts of interest.

Data availability. Data underlying the results presented in this paper are not publicly available at this time but may be obtained from the authors upon reasonable request.

Supplemental document. See Supplement 1 for supporting content.

References

1. N. J. Zabusky and M. D. Kruskal, "Interaction of "Solitons" in a Collisionless Plasma and the Recurrence of Initial States," Phys. Rev. Lett. **15**(6), 240–243 (1965).
2. J. Denschlag, "Generating solitons by phase engineering of a Bose-Einstein condensate," Science **287**(5450), 97–101 (2000).
3. Y. V. Kartashov, B. A. Malomed, and L. Torner, "Solitons in nonlinear lattices," Rev. Mod. Phys. **83**(1), 247–305 (2011).
4. J. P. Gordon, "Theory of the soliton self-frequency shift," Opt. Lett. **11**(10), 662 (1986).
5. J. H. Lee, J. Van Howe, C. Xu, and X. Liu, "Soliton self-frequency shift: Experimental demonstrations and applications," IEEE J. Select. Topics Quantum Electron. **14**(3), 713–723 (2008).
6. N. Nishizawa and T. Goto, "Compact System of Wavelength-Tunable Femtosecond Soliton Pulse Generation Using Optical Fibers," IEEE Photonics Technol. Lett. **11**(3), 325–327 (1999).
7. C. Xu and X. Liu, "Photonic analog-to-digital converter using soliton self-frequency shift and interleaving spectral filters," Opt. Lett. **28**(12), 986 (2003).
8. S. Oda and A. Maruta, "All-optical tunable delay line based on soliton self-frequency shift and filtering broadened spectrum due to self-phase modulation," Opt. Express **14**(17), 7895 (2006).
9. K. Tai, N. Bekki, and A. Hasegawa, "Fission of optical solitons induced by stimulated Raman effect," Opt. Lett. **13**(5), 392 (1988).
10. G. I. Stegeman and M. Segev, "Optical spatial solitons and their interactions: Universality and diversity," Science **286**(5444), 1518–1523 (1999).
11. S. Wabnitz, Y. Kodama, and A. B. Aceves, "Control of Optical Soliton Interactions," Opt. Fiber Technol. **1**(3), 187–217 (1995).
12. F. M. Mitschke and L. F. Mollenauer, "Experimental observation of interaction forces between solitons in optical fibers," Opt. Lett. **12**(5), 355 (1987).
13. A. Hause and F. Mitschke, "Reduced soliton interaction by Raman self-frequency-shift," Phys. Rev. A **80**(6), 063824 (2009).
14. S. Buch and G. P. Agrawal, "Intermodal soliton interaction in nearly degenerate modes of a multimode fiber," J. Opt. Soc. Am. B **33**(11), 2217 (2016).
15. X. Zhang, D. Pierangeli, C. Conti, D. Fan, and L. Zhang, "Control of soliton self-frequency shift dynamics via Airy soliton interaction," Opt. Express **26**(25), 32971 (2018).
16. P. Balla, S. Buch, and G. P. Agrawal, "Effect of Raman scattering on soliton interactions in optical fibers," J. Opt. Soc. Am. B **34**(6), 1247 (2017).
17. P. Balla and G. P. Agrawal, "Nonlinear interaction of vector solitons inside birefringent optical fibers," Phys. Rev. A **98**(2), 023822 (2018).
18. M. A. Eftekhar, Z. Sanjabi-Eznaveh, H. E. Lopez-Aviles, S. Benis, J. E. Antonio-Lopez, M. Kolesik, F. Wise, R. Amezcua-Correa, and D. N. Christodoulides, "Accelerated nonlinear interactions in graded-index multimode fibers," Nat. Commun. **10**(1), 1638 (2019).
19. G. Genty, C. M. de Sterke, O. Bang, F. Dias, N. Akhmediev, and J. M. Dudley, "Collisions and turbulence in optical rogue wave formation," Phys. Lett. A **374**(7), 989–996 (2010).
20. J. M. Dudley, F. Dias, M. Erkintalo, and G. Genty, "Instabilities, breathers and rogue waves in optics," Nat. Photonics **8**(10), 755–764 (2014).
21. S. A. Kolpakov, H. Kbashi, and S. V. Sergeyev, "Dynamics of vector rogue waves in a fiber laser with a ring cavity," Optica **3**(8), 870 (2016).
22. A. Armaroli, C. Conti, and F. Biancalana, "Rogue solitons in optical fibers: a dynamical process in a complex energy landscape?" Optica **2**(5), 497 (2015).
23. J. Herrmann, U. Griebner, N. Zhavoronkov, A. Husakou, D. Nickel, J. C. Knight, W. J. Wadsworth, P. S. Russell, and G. Korn, "Experimental evidence for supercontinuum generation by fission of higher-order solitons in photonic fibers," Phys. Rev. Lett. **88**(17), 173901 (2002).
24. D. V. Skryabin, F. Luan, J. C. Knight, and P. S. J. Russell, "Soliton self-frequency shift cancellation in photonic crystal fibers," Science **301**(5640), 1705–1708 (2003).
25. A. A. Voronin and A. M. Zheltikov, "Soliton self-frequency shift decelerated by self-steepening," Opt. Lett. **33**(15), 1723 (2008).
26. A. Bendahmane, O. Vanvincq, A. Mussot, and A. Kudlinski, "Control of the soliton self-frequency shift dynamics using topographic optical fibers," Opt. Lett. **38**(17), 3390 (2013).

27. R. Pant, A. C. Judge, E. C. Magi, B. T. Kuhlmey, M. de Sterke, and B. J. Eggleton, “Characterization and optimization of photonic crystal fibers for enhanced soliton self-frequency shift,” J. Opt. Soc. Am. B **27**(9), 1894 (2010).
28. Y. Xiang, X. Dai, S. Wen, J. Guo, and D. Fan, “Controllable Raman soliton self-frequency shift in nonlinear metamaterials,” Phys. Rev. A **84**(3), 033815 (2011).
29. Y. Hu, A. Tehranchi, S. Wabnitz, R. Kashyap, Z. Chen, and R. Morandotti, “Improved intrapulse Raman scattering control via asymmetric airy pulses,” Phys. Rev. Lett. **114**(7), 073901 (2015).
30. K. Krupa, A. Tonello, A. Barthélémy, T. Mansuryan, V. Couderc, G. Millot, P. Grelu, D. Modotto, S. A. Babin, and S. Wabnitz, “Multimode nonlinear fiber optics, a spatiotemporal avenue,” APL Photonics **4**(11), 110901 (2019).
31. K. Krupa, A. Tonello, B. M. Shalaby, M. Fabert, A. Barthélémy, G. Millot, S. Wabnitz, and V. Couderc, “Spatial beam self-cleaning in multimode fibres,” Nat. Photonics **11**(4), 237–241 (2017).
32. Z. Liu, L. G. Wright, D. N. Christodoulides, and F. W. Wise, “Kerr self-cleaning of femtosecond-pulsed beams in graded-index multimode fiber,” Opt. Lett. **41**(16), 3675 (2016).
33. K. Krupa, A. Tonello, A. Barthélémy, V. Couderc, B. M. Shalaby, A. Bendahmane, G. Millot, and S. Wabnitz, “Observation of Geometric Parametric Instability Induced by the Periodic Spatial Self-Imaging of Multimode Waves,” Phys. Rev. Lett. **116**(18), 183901 (2016).
34. G. P. Agrawal, “Invite paper: Self-imaging in multimode graded-index fibers and its impact on the nonlinear phenomena,” Opt. Fiber Technol. **50**, 309–316 (2019).
35. T. Hansson, A. Tonello, T. Mansuryan, F. Mangini, M. Zitelli, M. Ferraro, A. Niang, R. Crescenzi, S. Wabnitz, and V. Couderc, “Nonlinear beam self-imaging and self-focusing dynamics in a GRIN multimode optical fiber: theory and experiments,” Opt. Express **28**(16), 24005 (2020).
36. F. Mangini, M. Ferraro, M. Zitelli, V. Kalashnikov, A. Niang, T. Mansuryan, F. Frezza, A. Tonello, V. Couderc, A. B. Aceves, and S. Wabnitz, “Rainbow Archimedean spiral emission from optical fibres,” Sci. Rep. **11**(1), 13030 (2021).
37. W. H. Renninger and F. W. Wise, “Optical solitons in graded-index multimode fibres,” Nat. Commun. **4**(1), 1719 (2013).
38. M. Zitelli, M. Ferraro, F. Mangini, and S. Wabnitz, “Single-mode spatiotemporal soliton attractor in multimode GRIN fibers,” Photonics Res. **9**(5), 741 (2021).
39. M. Zitelli, F. Mangini, M. Ferraro, O. Sidelnikov, and S. Wabnitz, “Conditions for walk-off soliton generation in a multimode fiber,” Commun. Phys. **4**(1), 182 (2021).
40. L. G. Wright, D. N. Christodoulides, and F. W. Wise, “Spatiotemporal mode-locking in multimode fiber lasers,” Science **358**(6359), 94–97 (2017).
41. H. Qin, X. Xiao, P. Wang, and C. Yang, “Observation of soliton molecules in a spatiotemporal mode-locked multimode fiber laser,” Opt. Lett. **43**(9), 1982 (2018).
42. P. Horak and F. Poletti, “Multimode Nonlinear Fibre Optics: Theory and Applications,” Recent Progress in Optical Fiber Research pp. 3–25 (2012).
43. L. G. Wright, Z. M. Ziegler, P. M. Lushnikov, Z. Zhu, M. A. Eftekhar, D. N. Christodoulides, and F. W. Wise, “Multimode nonlinear fiber optics: Massively parallel numerical solver, tutorial, and outlook,” IEEE J. Sel. Top. Quantum Electron. **24**(3), 1–16 (2018).
44. A. B. Fallahkhair, K. S. Li, and T. E. Murphy, “Vector Finite Difference Modesolver for Anisotropic Dielectric Waveguides,” J. Lightwave Technol. **26**(11), 1423–1431 (2008).
45. R. H. Stolen, W. J. Tomlinson, H. A. Haus, and J. P. Gordon, “Raman response function of silica-core fibers,” J. Opt. Soc. Am. B **6**(6), 1159 (1989).
46. G. P. Agrawal, *Nonlinear fiber optics* (Academic press, 2013), 5 edit ed.
47. L. G. Wright, S. Wabnitz, D. N. Christodoulides, and F. W. Wise, “Ultrabroadband Dispersive Radiation by Spatiotemporal Oscillation of Multimode Waves,” Phys. Rev. Lett. **115**(22), 223902 (2015).
48. L. G. Wright, D. N. Christodoulides, and F. W. Wise, “Controllable spatiotemporal nonlinear effects in multimode fibres,” Nat. Photonics **9**(5), 306–310 (2015).